

# CONTROLLING THE DEFORMATION MECHANISM IN DISK SUPERALLOYS AT LOW AND INTERMEDIATE TEMPERATURES

Y. Yuan<sup>1</sup>, Y.F. Gu<sup>2</sup>, Z.H. Zhong<sup>2</sup>, T. Osada<sup>2†</sup>, T. Yokokawa<sup>1</sup>, H. Harada<sup>1</sup>

<sup>1</sup>Environment and Energy Materials Division,  
National Institute for Materials Science, 1-2-1 Sengen, Tsukuba 305-0047, Japan

<sup>2</sup>High Temperature Materials Unit,  
National Institute for Materials Science, Sengen 1-2-1, Tsukuba 305-0047, Japan

†now at Research Center for Green Materials Innovation, Yokohama National University, 79-1 Tokiwadai, Hodogaya-ku, Yokohama 240-8501, Japan

Keywords : Ni-Co-base superalloy; Tensile; Microstructure; Deformation mechanism; TMW-4M3

## Abstract

The newly developed TMW<sup>®</sup> disk superalloy exhibits better overall mechanical properties in the intended service temperature region (650-750 °C) than the most advanced cast & wrought disk alloy U720Li. Clarification of the underlying mechanisms is beneficial for designing advanced superalloys. Among the TMW alloys, TMW-4M3 has the best tensile strength and creep resistance. In this study, tensile tests of U720Li and TMW-4M3 were conducted at temperatures ranging from 25 °C to 750 °C. The deformation microstructures have been investigated by transmission electron microscopy (TEM). Dislocation activity, involving anti-phase boundary (APB), was the dominant mechanism in U720Li up to 725 °C. However, the transition of deformation mechanisms from dislocation pairs cutting to stacking fault (SF) shearing and deformation twinning was observed in TMW-4M3. A concise model related to the increased surface energy is put forward to describe the competing mechanisms. It is found that APB energy, SF energy (SFE), and volume fraction of tertiary  $\gamma'$  have important influence on the transition of deformation mechanisms. The controlling of deformation mechanism by alloy design is discussed.

## Introduction

Ni-base superalloys are extensively used in aircraft engines and land-based gas turbines, owing to their unique high temperature mechanical properties. Super-dislocations play an important role during the deformation of disk superalloys, which usually interact with  $\gamma'$  precipitates in two different ways at low (25-600 °C) to intermediate temperatures (600-800 °C), i.e., cutting the precipitates by coupled  $a/2\langle 110 \rangle$  ( $a$  is the lattice constant) dislocation pairs or dissociating into super-partial dislocations [1]. The former creates anti-phase boundary (APB) in the  $\gamma'$  precipitates, and the latter forms stacking fault (SF). The mechanism favored by the specific alloy depends on the energy status in the system, which is related to microstructure, deformation condition and temperature. In disk superalloys, usually, dislocation pairs cutting mechanism prevails at temperatures below 600 °C [2-4]. Planar defects, such as SF and deformation twin, occur in the temperature range of 600-800 °C. Above 800 °C, dislocation climb is the dominant mechanism [1]. Kolbe reported the transition of deformation mechanisms from dislocation pairs cutting to deformation twinning at 780 °C in NIMONIC 105 and NIMONIC PE 16 [5]. However, the transition

of deformation mechanisms associated with APB energy and SF energy is not yet fully understood.

At National Institute for Materials Science, Japan, a new cast & wrought Ni-Co-base disk superalloy, TMW-4M3, has been developed for applications at elevated temperatures up to 725 °C [6-12]. It has been reported that TMW-4M3 has comparable yield strength with U720Li at room temperature, but superior yield strength in the service temperature region from 650 °C to 750 °C [6]. TMW-4M3 has higher APB energy and lower SF energy than U720Li. The relationship between these energies and higher yield strength at intermediate temperatures need further investigation.

In the present study, the deformation microstructures of U720Li and TMW-4M3 after tensile tests at low (25 °C) to intermediate temperature (750 °C) have been investigated by transmission electron microscopy (TEM). A concise model related to the increased interface energy is put forward to describe the transition of deformation mechanisms. The controlling of deformation mechanism by alloy design is discussed.

## Experimental

The detailed processes of preparing two alloy ingots can be found elsewhere [6]. All specimens were cut from the forged pancakes (440 mm in diameter and 65 mm in thickness), then heat treated as follows: 1100 °C/4 h/oil quenching (OQ), then aging at 650 °C /24 h/OQ +760 °C/16 h/OQ. Tensile tests were performed at 25 °C (room temperature, RT), 400 °C, 650 °C, 700 °C, 725 °C, and 750 °C according to ASTM E8/E21. Besides the ruptured tests, three interrupted tests with 1.0% plastic strain for TMW-4M3 at 25 °C, 650 °C, and 725 °C were selected. After the mechanical tests, TEM discs with thickness of around 300  $\mu\text{m}$  were cut from the deformed samples perpendicular to the stress axis. Then the discs were manually ground to 50  $\mu\text{m}$  and perforated by twin-jet electro-polisher at 40 V/18 mA and -10 °C. The electrolyte consisted of 225 ml acetic acid, 225 ml butylcellosolve, and 50 ml perchloric acid. The microstructures of specimens were investigated using a Tecnai 20 microscope operated at 200 kV.

Burgers vectors of dislocations were determined using  $\mathbf{g}\cdot\mathbf{b}$  criterion. In our observations, the deviation vector ( $\mathbf{s}$ ) was always kept positive and the deviation parameter ( $\xi_{\mathbf{g}} \cdot \mathbf{s}$ ) was maintained to be larger than 0.7. For different values of  $\mathbf{g}\cdot\mathbf{b}$ , the visibility and invisibility of partial dislocation on the one side of SF are summarized as follows:

Table I Nominal Chemical Compositions of TMW-4M3 and U720Li (wt.%)

Alloy	Ni	Cr	Mo	W	Co	Ti	Al	C	B	Zr
TMW-4M3	Bal.	13.5	2.8	1.2	25.0	6.2	2.3	0.03	0.02	0.03
U720Li	Bal.	16.3	3.1	1.3	14.8	4.8	2.4	0.03	0.02	0.03

$\mathbf{g \cdot b} = 0, \pm 1/3, -2/3, +4/3$ , partial dislocation invisible  
 $\mathbf{g \cdot b} = +2/3, +4/3, \pm 1$ , etc. partial dislocation visible  
 The signs for 2/3 and 4/3 should be reversed for the partial dislocation lying to another side of SF [13].

## Results and discussion

### Initial microstructures

The chemical compositions of two alloys are listed in Table I. TMW-4M3 contained higher Co content than U720Li. The microstructures of two alloys before tensile tests were similar and have been described in reference [6]. Both alloys consisted of  $\gamma$  matrix and  $\gamma'$  precipitates. The total volume fraction of  $\gamma'$  precipitates in TMW-4M3 and U720Li was 49.5% and 45.0%, respectively.

### Tensile properties

For each alloy, two specimens were tested at each temperature. Figure 1(a) shows the average tensile properties of two superalloys at various temperatures. The ultimate tensile strength

( $\sigma_b$ ) of TMW-4M3 is significantly higher than that of U720Li in the temperature range of 25-725 °C. TMW-4M3 has comparable yield strengths ( $\sigma_{0.2}$ ) with U720Li at temperatures below 650 °C, whereas it has higher  $\sigma_{0.2}$  than U720Li in the temperature range of 650-750 °C. With increasing temperature, the discrepancy of  $\sigma_{0.2}$  between TMW-4M3 and U720Li gradually increases and reaches the maximum at 750 °C, i.e., 10% higher (see Figure 1(b)).

### Microstructures after tensile deformation

Deformation microstructures of U720Li: The representative microstructures of U720Li after tensile rupture at RT, 650 °C, and 725 °C are shown in Figure 2. Dislocation slip bands were present at RT, and Orowan dislocation loops were frequently observed at 650 °C. With increasing temperature to 725 °C, dislocation slip combining climb was the main deformation mode, and few stacking faults were formed. These results indicate that dislocation activity, mainly dislocation-coupled APB shearing, is the dominant mechanism in U720Li up to 725 °C. Our observation is in agreement with Gopinath's report [14].

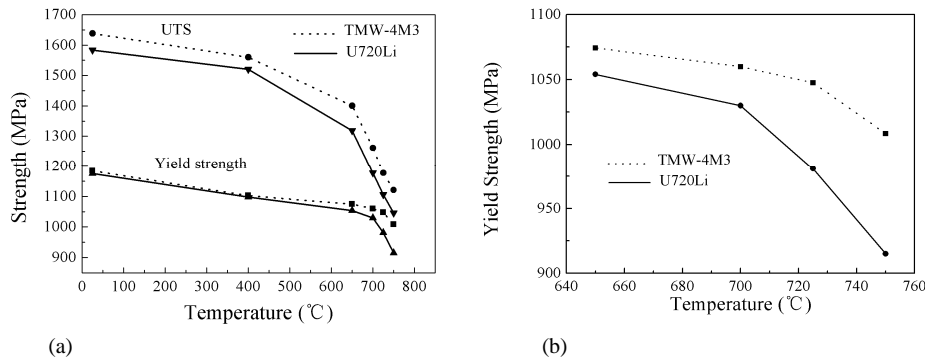


Figure 1. (a) Average tensile properties of TMW-4M3 and U720Li at various temperatures. (b) Yield strength of TMW-4M3 and U720Li in the temperature range of 650-750 °C

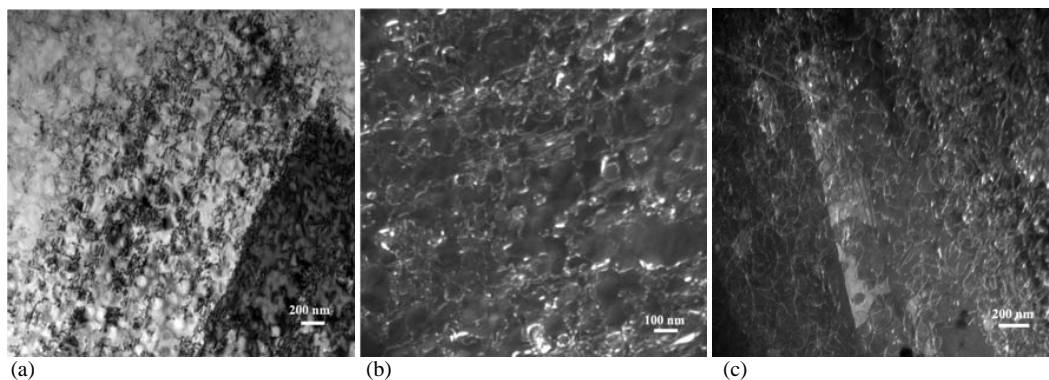


Figure 2. Ruptured microstructures (samples were cut far from the ruptured surface) of U720Li at: (a) RT, dislocation slip bands were present; (b) 650 °C, Orowan dislocation loops were frequently observed; and (c) 725 °C, Dislocation slip combining climb was the main deformation mode. Few stacking faults were formed.

### Deformation microstructures of TMW-4M3:

*Microstructures after 1.0% plastic strain:* Figure 3 shows the microstructures of TMW-4M3 with 1.0% plastic strain at RT, 650 °C, and 725 °C. Dislocation pairs cut through the  $\gamma'$  precipitates at RT, as shown in Figure 3(a). The Burgers vector of the paired dislocations involving the creation of APB in the  $\gamma'$  precipitates was determined to be  $a/2\langle 110 \rangle$  by contrast analysis. Paired dislocations interacting with the  $\gamma'$  precipitates are usually active in superalloys when deformed at low temperature [15, 4]. The precipitate size and volume fraction are controlling parameters to determine the specific mechanism, namely, weakly or strongly coupled dislocations. For present case, the size of secondary  $\gamma'$  precipitates was about 100 nm, several times larger than the spacing between these paired dislocations in Figure 3(a). The spacing between weakly coupled dislocations is defined to be much larger than the precipitate size. It is therefore inferred that the dislocation pairs in Figure 3 (a) are strongly coupled.

At 650 °C, numerous SFs can be seen in Figure 3(b). The length of most SFs was a few tens of nanometers. The SFs were verified to lie on two variants of  $\{111\}$  planes. At 725 °C, long deformation twins sheared both the matrix and the  $\gamma'$  precipitates, as shown in Figure 3(c). Twin reflections can be clearly observed in the inset [110] selected area diffraction (SAD). The thickness of deformation twins was around 10 nm. These results indicate that increasing temperature promotes the transition of SF shearing to deformation twinning.

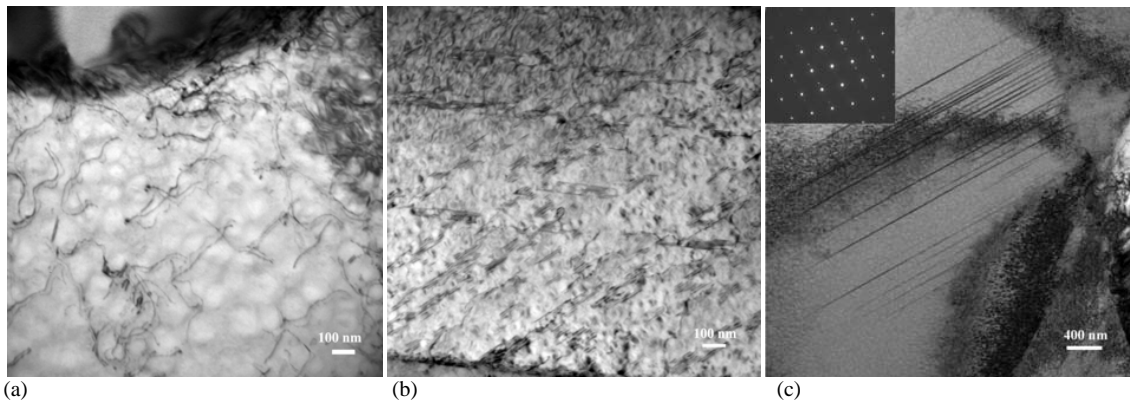


Figure 3. Microstructures of TMW-4M3 with 1.0% plastic strain. (a) At RT, dislocation pairs cut the  $\gamma'$  precipitates; (b) At 650 °C, partial dislocations sheared the  $\gamma'$  precipitates, leaving short stacking faults behind; (c) At 725 °C, numerous deformation twins sheared both the matrix and the  $\gamma'$  precipitates, inset SAD showing twin reflections.

*Microstructures after rupture:* At RT, comparing Figure 4(a) with Figure 3(a), one can find that the dislocation density in the ruptured sample increased dramatically. Very few SFs were observed, which indicates that dislocation dissociation even at the final deformation stage is still difficult. The deformation microstructure at 400 °C, Figure 4(b), is similar to that at RT.

At 650 °C, the SF extended over a few hundreds of nanometers. Figure 4(c) shows the SFs close to the edge-on orientation. The reflection spots originated from deformation twins were absent in the inset SAD. Comparing Figure 4(c) with Figure 3(b), it is concluded that larger strain can promote the extending of SF.

At 700 and 725 °C, lots of deformation twins at nano-scale were present and had transversed across entire grains. Typical microstructures are illustrated in Figure 4(d) and (e). The diffraction spots from twins are marked by arrows in the inset [110] SAD of Figure 4(d). The bright laths in Figure 4(e) are deformation twins, imaged by selecting twin reflection.

### Nature of SF and dislocation dissociation in TMW-4M3

The nature of SF in TMW-4M3 was determined by contrast analysis under two beam conditions. Figure 5 (a) and (b) show the BF and DF images of SF in the sample deformed at 650 °C, respectively. Beam direction is along  $[\bar{1}10]$ . In Figure 5(a), both the outmost left and right fringe are dark, operating vector  $(\bar{1}\bar{1}\bar{1})$  points toward the dark fringe of SF. In Figure 5(b), operating vector is (111), the outmost left fringe is bright, whereas the outmost right fringe is dark,  $(\bar{1}\bar{1}\bar{1})$  points toward the bright fringe of SF. According to the commonly used rules [16], the SF is intrinsic.

The dislocation dissociation in interrupted sample deformed at 650 °C was analyzed in detail. Figure 6 shows the representative micrographs used for the analysis of Burgers vectors of partials (1 and 2) bounding SF. The fault plane determined by trace line analysis is  $(1\bar{1}1)$ . In Figure 6(a), both partial 1 and 2 are visible, while only partial 2 is visible in Figure 6(b). Experimental

observations of visibility/invisibility of partials under various two beam conditions are given in Table II. The results indicate that the Burgers vectors of two partials bounding SF are of  $a/6[\bar{1}12]$  and  $a/3[21\bar{1}]$ , respectively. The dislocation dissociation is as follows:

$$a/2[110] = a/6[\bar{1}12] + SF + a/3[21\bar{1}]$$

The leading partial may have the Burgers vector of  $a/3[21\bar{1}]$ , which sheared the matrix and precipitates continuously, leaving intrinsic SF behind. Because Shockley partial dislocation shearing  $\gamma'$  precipitate forms complex SF with high energy in the  $\gamma'$  precipitate. It is energetically unfavorable. So the trailing partial  $a/6[\bar{1}12]$  was left at  $\gamma/\gamma'$  interface. Similar dislocation processes have been reported in IN738LC alloy under monotonic loading at

elevated temperatures and in C263 alloy after creep deformation at 800 °C [17, 18].

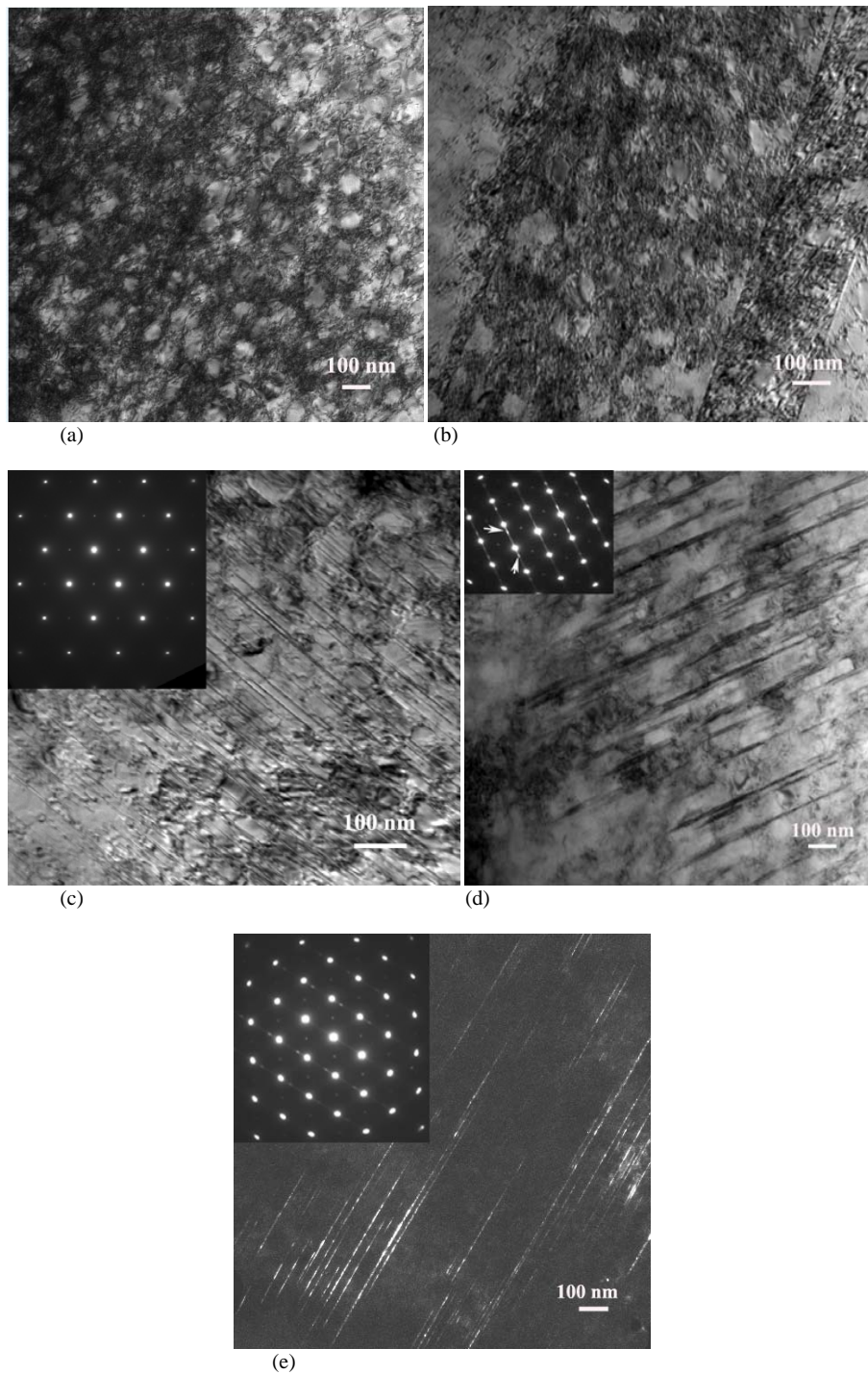


Figure 4. Microstructures after tensile rupture at various temperatures. Dislocations slipping was the dominant mechanism at RT (a) and 400 °C (b); SF developed to be the main mechanism at 650 °C (c); deformation twinning evolved to be the controlling mechanism at 700 °C (d) and 725 °C (e).

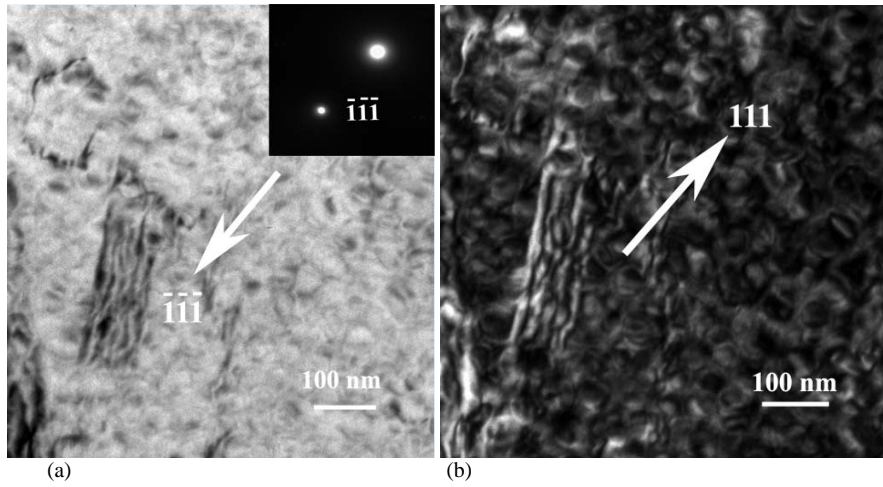


Figure 5. (a) BF image of SF. Zone axis is  $[\bar{1}\bar{1}0]$ . Operating vector  $(\bar{1}\bar{1}\bar{1})$  points toward the dark fringe of SF. (b) DF image of SF. Operating vector is  $(111)$ , and  $(\bar{1}\bar{1}\bar{1})$  points toward the bright fringe (left side) of SF.

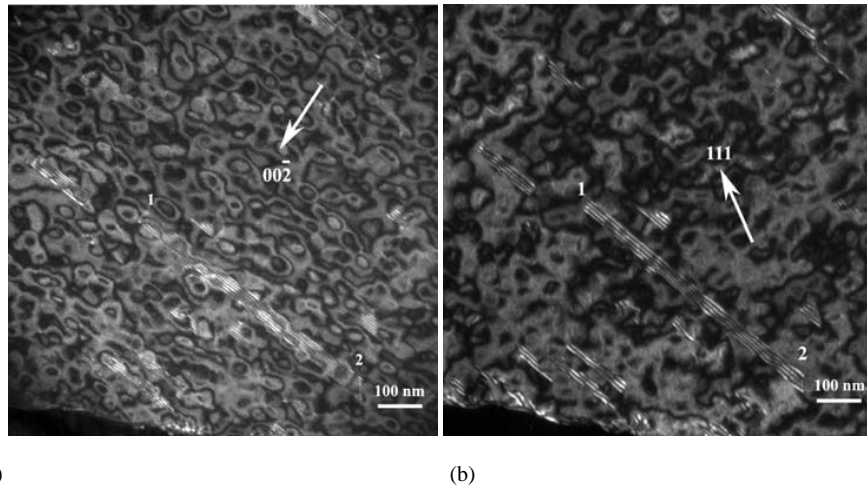


Figure 6. Representative micrographs corresponding to Table II used for the analysis of Burgers vectors of partial dislocations (1 and 2) bounding SF. (a)  $BD=[\bar{1}\bar{1}0]$ ,  $\mathbf{g} = (00\bar{2})$ ; (b)  $BD=[\bar{1}\bar{1}0]$ ,  $\mathbf{g} = (111)$ .

Table II Experimental Observations of Visibility (v)/Invisibility (i) of Partials Under Different Two Beam Imaging Conditions. Fault Plane Is  $(1\bar{1}1)$ . Sample Deformed at 650 °C.

$\mathbf{g}$	Observations of partial 1	$\mathbf{g}\cdot\mathbf{b}_{p1}$ $\mathbf{b}_{p1}=a/6[\bar{1}\bar{1}2]$	Observations of partial 2	$\mathbf{g}\cdot\mathbf{b}_{p2}$ $\mathbf{b}_{p2}=a/3[21\bar{1}]$
$00\bar{2}$	v	-2/3	v	+2/3
$002$	weak	+2/3	i	-2/3
$11\bar{1}$	i	-1/3	i	+4/3
$\bar{1}\bar{1}1$	i	+1/3	v	-4/3
$111$	i	+1/3	v	+2/3
$\bar{1}\bar{1}\bar{1}$	i	-1/3	i	-2/3
$02\bar{2}$	i	-1/3	i	+4/3
$0\bar{2}2$	i	+1/3	v	-4/3
$1\bar{1}\bar{3}$	i	+2/3	weak	-2/3
$20\bar{2}$	i	-1/3	weak	-2/3

### Deformation mechanism

The dislocation pairs cutting mechanism (APB shearing mechanism) and SF shearing mechanism, schematically shown in Figure 7(a) and (b), are two competing deformation modes. As mentioned before, the former prevails in superalloys at temperatures below 600 °C, while the latter is usually observed at elevated temperatures. For the sheared area, APB is created in both the tertiary  $\gamma'$  precipitates and small part of secondary  $\gamma'$  precipitates when coupled dislocations movement is active. SF is

formed in the matrix, secondary and tertiary  $\gamma'$  precipitates when SF shearing is the main deformation mechanism. Here, we put forward a concise model to describe the two processes. The increased surface energy per deformed unit area corresponding to the two mechanisms can be expressed as follows:

$$\text{APB shearing mechanism, } \Delta E = \gamma_{\text{APB}}(f_{\gamma_{\text{III}}} + \theta f_{\gamma_{\text{II}}}) \quad (1)$$

$$\text{SF shearing mechanism, } \Delta E = \gamma_{\text{SF}}^{\text{p}}(f_{\gamma_{\text{III}}} + f_{\gamma_{\text{II}}}) + \gamma_{\text{SF}}^{\text{m}} f_{\text{m}} \quad (2)$$

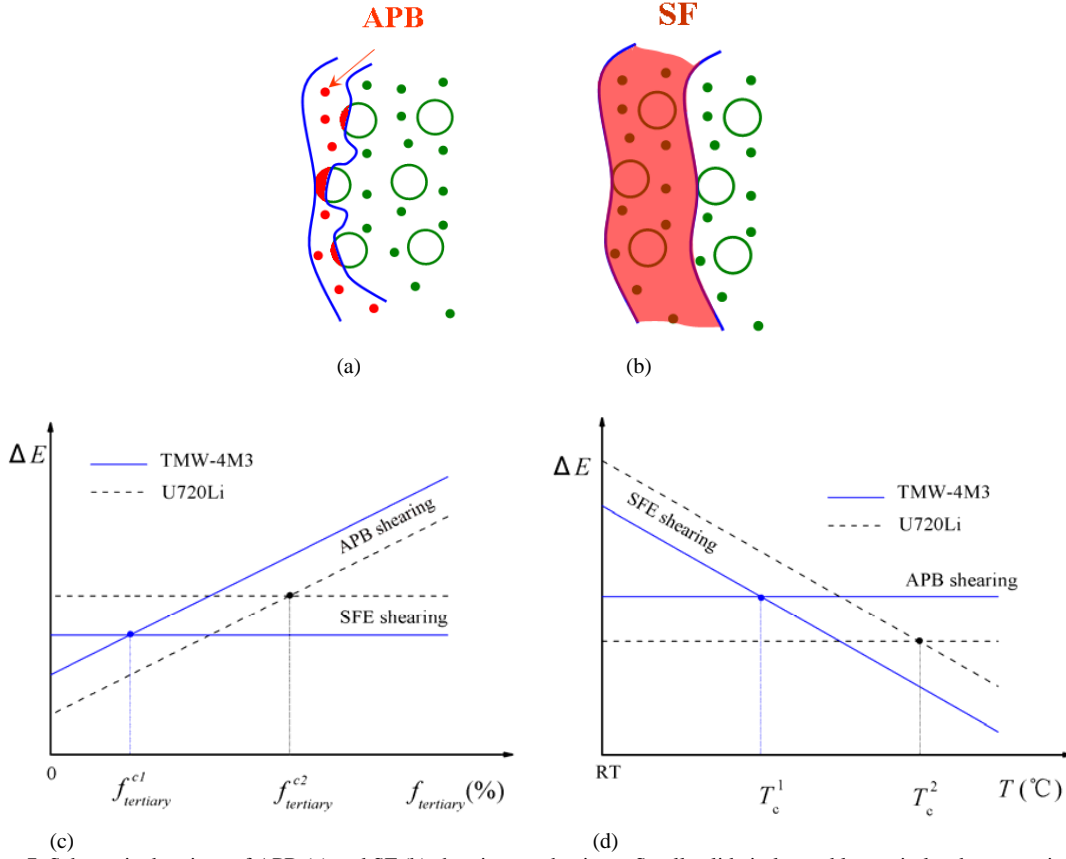


Figure 7. Schematic drawings of APB (a) and SF (b) shearing mechanisms. Small solid circles and large circles denote tertiary and secondary  $\gamma'$  precipitates, respectively. (c) The  $\Delta E$  corresponding to APB shearing and SF shearing mechanisms as a function of  $f_{\text{tertiary}}$ . (d) The  $\Delta E$  corresponding to APB shearing and SF shearing mechanisms as a function of temperature (T).

Where

$\Delta E$  is the increased surface energy per deformed unit area in system,

$\gamma_{\text{APB}}$  is the APB energy of  $\gamma'$  precipitates,  
 $f_{\gamma_{\text{III}}}$  is the volume fraction of tertiary  $\gamma'$  precipitates,  
 $\theta$  is a coefficient between zero and one,  
 $f_{\gamma_{\text{II}}}$  is the volume fraction of secondary  $\gamma'$  precipitates,  
 $\gamma_{\text{SF}}^{\text{p}}$  is the stacking fault energy of  $\gamma'$  precipitates,  
 $\gamma_{\text{SF}}^{\text{m}}$  is the stacking fault energy of  $\gamma$  matrix,  
 $f_{\text{m}}$  is the volume fraction of  $\gamma$  matrix.

Note that the  $\Delta E$  depends on the microstructure, APB energy of  $\gamma'$  precipitates, and SF energy of both matrix and precipitates.

For equation (1), the  $\Delta E$  is linear to  $f_{\gamma_{\text{III}}}$  by assuming that  $\theta f_{\gamma_{\text{II}}}$  is a constant (very small but not zero in case of low strain), as illustrated in Figure 7(c). For SF shearing mechanism, the  $\Delta E$  is a constant by assuming that the  $\gamma_{\text{SF}}^{\text{p}}$  is equal to  $\gamma_{\text{SF}}^{\text{m}}$  and volume fraction of primary  $\gamma'$  is a constant, as shown in Figure 7(c). The two lines have an intersection point, as indicated in Figure 7(c).

Table III The Value of Various Parameters and Calculated Results of  $\Delta E$  ( $\text{mJ}\cdot\text{m}^{-2}$ ) at RT

Alloy	$f_{\gamma\text{II}}$	$f_{\gamma\text{III}}^{\text{a}}$	$f_{\text{m}}$	$\theta$	$\gamma_{\text{APB}}^{\text{b}}$	$\gamma_{\text{SF}}^{\text{p,c}}$	$\gamma_{\text{SF}}^{\text{m,d}}$	$\Delta E(\text{APB})$	$\Delta E(\text{SF})$
TMW-4M3	0.32	0.015	0.505	0	180	19.9	19.9	2.7	16.7
U720Li	0.294	0.025	0.55	0	150	35.9	35.9	3.8	31.2

<sup>a</sup> The total volume fraction of  $\gamma'$  in TMW-4M3 and U720Li was 0.495 and 0.45, respectively, calculated by Thermal-cal program with a Ni-RUMN database. The volume fraction of primary  $\gamma'$  in TMW-4M3 and U720Li was examined by SEM to be around 0.16 and 0.13, respectively.

<sup>b</sup> Reference 19.

<sup>c</sup> The stacking fault energy of  $\gamma'$  precipitates is unknown, it is assumed to be equal to  $\gamma_{\text{SF}}^{\text{m}}$ .

<sup>d</sup> The  $\gamma_{\text{SF}}^{\text{m}}$  of TMW-4M3 and U720Li is  $19.9 \pm 2.5 \text{ mJ}\cdot\text{m}^{-2}$  and  $35.9 \pm 3.7 \text{ mJ}\cdot\text{m}^{-2}$ , respectively, determined via high resolution TEM.

This point means a critical volume fraction of tertiary  $\gamma'$  ( $f_{\text{tertiary}}^{\text{c}}$ ). Below the  $f_{\text{tertiary}}^{\text{c}}$ , APB shearing mechanism is active. Above the  $f_{\text{tertiary}}^{\text{c}}$ , SF shearing mechanism is dominant.

The influence of temperature on the deformation mechanism can be interpreted by considering the temperature dependence of  $\Delta E$ . The APB energy is assumed to be nearly constant from RT to 700 °C, while SFE decreases within this temperature range [20, 21]. The  $\Delta E$  corresponding to APB shearing (equation (1)) is therefore a constant, however, it decreases with increasing temperature in case of SF shearing mechanism. The temperature dependence of  $\Delta E$  is plotted in Figure 7(d). There exists a critical temperature  $T_{\text{c}}$ . Below the  $T_{\text{c}}$ , the APB shearing mechanism is favored, while the SF shearing mechanism is expected above the  $T_{\text{c}}$ .

According to equation (1) and (2), APB energy, SFE, and  $f_{\gamma\text{III}}$  have great influence on  $f_{\text{tertiary}}^{\text{c}}$  and  $T_{\text{c}}$ , which are corresponding to the transition of deformation mechanisms. Higher APB energy and lower SFE cause the shift of  $f_{\text{tertiary}}^{\text{c}}$  and  $T_{\text{c}}$  to left side, as inferred from Figure 7. Though the volume fraction of tertiary  $\gamma'$  is small, it does affect the deformation processes. Locq et al. have reported that the tertiary  $\gamma'$  may play a major role in the shearing process [22], which is in agreement with our proposal.

As far as TMW-4M3 and U720Li are concerned with this model, the  $\Delta E$  at RT can be roughly estimated. The value of various parameters and calculated results are listed in Table III. The  $\Delta E$  corresponding to APB and SF shearing mechanisms in TMW-4M3 is 2.7 and 16.7  $\text{mJ}\cdot\text{m}^{-2}$ , and 3.8 and 31.2  $\text{mJ}\cdot\text{m}^{-2}$  in U720Li, respectively. For both alloys, the  $\Delta E$  corresponding to SF shearing mechanism is much greater than that corresponding to APB shearing mechanism. So APB shearing mechanism was favored at RT, which is consistent with the experimental observation.

When compared TMW-4M3 with U720Li, it is found that TMW-4M3 has higher APB energy and lower SFE than U720Li. The APB energy is higher at higher Ti to Al ratios [23]. Because TMW-4M3 has higher Ti to Al ratio than U720Li (see Table I), it is reasonable to assume that TMW-4M3 has higher APB energy than U720Li. The SFE of  $\gamma$  matrix in TMW-4M3 and U720Li has been determined to be  $19.9 \pm 2.5 \text{ mJ}\cdot\text{m}^{-2}$  and  $35.9 \pm 3.7 \text{ mJ}\cdot\text{m}^{-2}$ , respectively [24]. High APB energy and lower SFE result in the  $f_{\text{tertiary}}^{\text{c2}} > f_{\text{tertiary}}^{\text{c1}}$  and  $T_{\text{c}}^2 > T_{\text{c}}^1$  (see Figure 7(c) and (d)). The  $T_{\text{c}}$  in TMW-4M3 may be around 650 °C. So we can observe the transition of various deformation mechanisms in the temperature range of 25-725 °C in TMW-4M3. In contrast, only dislocation

slip and/or climb prevailed in U720Li up to 725 °C, which implies that the  $T_{\text{c}}$  in U720Li may be higher than 725 °C.

It is demonstrated that the deformation mechanisms in TMW-4M3 and U720Li are different at low to intermediate temperatures depending on the energy status. The mechanical behavior is closely associated with the deformation mechanisms. In TMW-4M3, the enhanced yield strength in the temperature range of 650-750 °C is just corresponding to SF shearing and deformation twinning. Previous results have demonstrated that twin strengthening contributes to the enhanced strength in TMW-4M3 [25, 26]. Here, the deformation processes involving planar defects, such as SFs and deformation twins, may be partly responsible for the enhanced yield strength of TMW-4M3 at service temperatures (650-750 °C). So controlling the deformation mechanism in disk superalloys seems to be a very useful method for improving the mechanical properties. Our results show that it is possible to control the deformation mechanism. For example, the APB energy and SFE, intrinsic parameters of materials, can be tailored by chemical composition design. The volume fraction of tertiary  $\gamma'$  can be adjusted by composition and heat treatment. Further investigation is needed to clarify possible other factors that may have great influence on the transition of deformation mechanisms.

## Summary

The deformation microstructures of alloy U720Li and TMW-4M3 after tensile tests at various temperatures have been studied by TEM. The main conclusions are as follows:

(1) Dislocation activity, mainly APB shearing, was the dominant mechanism in U720Li up to 725 °C.

(2) In TMW-4M3, APB shearing mechanism was dominant at RT and 400 °C, while intrinsic SFs shearing both the  $\gamma$  matrix and  $\gamma'$  precipitates operated at 650 °C. Moreover, deformation twinning occurred above 700 °C.

(3) A model related to the increased interface energy is put forward to describe the APB shearing and SF shearing mechanisms. The analysis indicates that there is a critical value, that is  $f_{\text{tertiary}}^{\text{c}}$  and  $T_{\text{c}}$ . APB is favored when  $f_{\text{tertiary}}^{\text{c}}$  and temperature are below the critical value, otherwise SF is favored.

(4) APB and SF energy have great influence on  $f_{\text{tertiary}}^{\text{c}}$  and  $T_{\text{c}}$ , which are corresponding to the transition of deformation mechanisms. Higher APB energy and lower SFE decrease the transition temperature from APB shearing to SF shearing mechanism.

(5) The volume fraction of tertiary  $\gamma'$ , APB energy, and SFE are important parameters for controlling the deformation mechanism in disk superalloys.

## References

1. L. Kovarik, R.R. Unocic, J. Li, P. Sarosi, C. Shen, Y. Wang, and M.J. Mills, "Microtwinning and other shearing mechanisms at intermediate temperatures in Ni-based superalloys", *Prog. Mater. Sci.*, 54 (2009), 839-873.
2. E. Nembach, K. Suzuki, M. Ichihara, and S. Takeuchi, "In situ deformation of the  $\gamma'$  hardened superalloy Nimonic PE16 in high-voltage electron microscopes", *Phil. Mag. A*, 51 (1985), 607-618.
3. E. Nembach, K. Suzuki, M. Ichihara, and S. Takeuchi, "HVEM in situ observation of dislocation processes in the  $\gamma'$ -hardened superalloy Nimonic 105", *Phil. Mag. A*, 56 (1987), 439-451.
4. B. Reppich, P. Schepp, and G. Wehner, "Some new aspects concerning particle hardening mechanisms in  $\gamma'$  precipitating Nickel-base alloys —II. Experiments", *Acta Metall.*, 30 (1982), 95-104.
5. M. Kolbe, "The high temperature decrease of the critical resolved shear stress in nickel-base superalloys", *Mater. Sci. Eng. A*, 319-321 (2001), 383-387.
6. Y.F. Gu, T. Fukuda, C. Cui, H. Harada, A. Mitsuhashi, T. Yokokawa, J. Fujioka, Y. Koizumi, and T. Kobayashi, "Comparison of mechanical properties of TMW alloys, new generation of cast-and-wrought superalloys for disk applications", *Metall. Mater. Trans. A*, 40 (2009), 3047-3050.
7. Y.F. Gu, C. Cui, H. Harada, T. Fukuda, D. Ping, A. Mitsuhashi, K. Kato, T. Kobayashi, and J. Fujioka, "Development of Ni-Co-base alloys for high-temperature disk applications", *Superalloys 2008*, Eds. Roger C. Reed et al., (Warrendale, PA, U.S.A.:TMS, 2008), 53-61.
8. H. Harada, Y.F. Gu, C.Y. Cui, M. Osawa, A. Sato, and T. Kobayashi, "Heat-resistant superalloy", European patent 1842934 B1.
9. C.Y. Cui, Y.F. Gu, D.H. Ping, and H. Harada, "Phase constituents in Ni-Al-Co-Ti quaternary alloys", *Intermetallics*, 16 (2008), 910-916.
10. C.Y. Cui, Y.F. Gu, D.H. Ping, H. Harada, and T. Fukuda, "The evolution of eta phase in Ni-Co base superalloys", *Mater. Sci. Eng. A*, 485 (2008), 651-656.
11. Y.F. Gu, H. Harada, C.Y. Cui, D.H. Ping, A. Sato, and J. Fujioka, "New Ni-Co-base disk superalloys with higher strength and creep resistance", *Scripta Mater.*, 55 (2006), 815-818.
12. C.Y. Cui, Y.F. Gu, H. Harada, and A. Sato, "Microstructure and yield strength of UDIMET 720Li alloyed with Co-16.9 wt pct Ti", *Metall. Mater. Trans. A*, 36 (2005), 2921-2927.
13. G.S. Hillier, C.M.F. Rae, and H.K.D.H. Bhadeshia, "Extrinsic and intrinsic nodes in the gamma prime phase of a single crystal superalloy", *Acta Metall.*, 36 (1988), 95-109.
14. K. Gopinath, A.K. Gogia, S.V. Kamat, R. Balamuralikrishnan, and U. Ramamurty, "Tensile Properties of Ni-Based Superalloy 720Li: Temperature and Strain Rate Effects", *Metall. Mater. Trans. A*, 39 (2008), 2340.
15. M.P. Jackson, and R.C. Reed, "Heat treatment of UDIMET 720Li: the effect of microstructure on properties", *Mater. Sci. Eng. A*, 259 (1999), 85-97.
16. J. Van Landuyt, R. Gevers, and S. Amelinckx, "On the determination of the nature of stacking faults in f.c.c. metals from the bright field image", *Phys. stat. sol.*, 18 (1966), 167-172.
17. D. Mukherji, F. Jiao, W. Chen, and R.P. Wahi, "Stacking fault formation in  $\gamma'$  phase during monotonic deformation of IN738LC at elevated temperatures", *Acta Metall.*, 39 (1991), 1515-1524.
18. Y.H. Zhang, Q.Z. Chen, and D.M. Knowles, "Mechanism of dislocation shearing of  $\gamma'$  in fine precipitate strengthened superalloy", *Mater. Sci. Technol.*, 17 (2001), 1551-1555.
19. F. Diologent, and P. Caron, "On the creep behavior at 1033K of new generation single-crystal superalloys", *Mater. Sci. Eng. A*, 385 (2004), 245-257.
20. W.W. Milligan, and S.D. Antolovich, "The Mechanisms and Temperature Dependence of Superlattice Stacking Fault Formation in the Single-Crystal Superalloy PWA 1480", *Metall. Trans. A*, 22 (1991), 2309-2318.
21. F. Pettinari, J. Douin, G. Saada, P. Caron, A. Coujou, and N. Clément, "Stacking fault energy in short-range ordered  $\gamma'$ -phases of Ni-based superalloys", *Mater. Sci. Eng. A*, 325 (2002), 511-519.
22. D. Locq, P. Caron, S. Raujol, F. Pettinari-Strumel, A. Coujou, and N. Clément, "On the role of tertiary  $\gamma'$  precipitates in the creep behavior at 700 °C of a PM disk superalloy", *Superalloys 2004*, Eds. K.A. Green et al., (Warrendale, PA, U.S.A.:TMS, 2004), 179-187.
23. D. Raynor, and J.M. Silcock, "Strengthening mechanisms in  $\gamma'$ -precipitating alloys", *Metal Sci. J.*, 4 (1970), 121.
24. Y. Yuan, Y.F. Gu, C.Y. Cui, T. Osada, Z.H. Zhong, T. Tetsui, T. Yokokawa, and H. Harada, "Influence of Co content on stacking fault energy in Ni-Co base disk superalloys", *J. Mater. Res.*, 26 (2011), 2833.
25. Y. Yuan, Y.F. Gu, T. Osada, Z.H. Zhong, T. Yokokawa, and H. Harada, "A new method to strengthen turbine disc superalloys at service temperatures", *Scripta Mater.*, In press (2012) doi: 10.1016/j.scriptamat.2012.01.025.
26. Y. Yuan, Y.F. Gu, C.Y. Cui, T. Osada, T. Yokokawa, and H. Harada, "A novel strategy for the design of advanced engineering alloys — strengthening turbine disk superalloys via twinning Structures", *Adv. Eng. Mater.*, 13 (2011), 296.